A Boundary Condition Relaxation Algorithm for Strongly Coupled, Ablating Flows including Shape Change

Peter A. Gnoffo[*] and Christopher O. Johnston[†]

NASA Langley Research Center, Hampton, VA 23681-2199

Implementations of a model for equilibrium, steady-state ablation boundary conditions are tested for the purpose of providing strong coupling with a hypersonic flow solver. The objective is to remove correction factors or film cooling approximations that are usually applied in coupled implementations of the flow solver and the ablation response. Three test cases are considered - the IRV-2, the Galileo probe, and a notional slender, blunted cone launched at 10 km/s from the Earth's surface. A successive substitution is employed and the order of succession is varied as a function of surface temperature to obtain converged solutions. The implementation is tested on a specified trajectory for the IRV-2 to compute shape change under the approximation of steady-state ablation. Issues associated with stability of the shape change algorithm caused by explicit time step limits are also discussed.

I. Introduction

Exploration missions to planets or moons supporting an atmosphere and return missions to Earth usually involve high speed entry at hyperbolic speeds (greater than escape velocity). Atmospheric drag is used to slow the vehicle to enable aerocapture or landing and save mass associated with fuel burn of retro-propulsion prior to entry. Simulation of the aerothermal environment surrounding a vehicle traveling at hyperbolic velocities through a planetary atmosphere requires coupling of the high temperature flow field with the thermal protection system (TPS) material response (ablation, shape change) and with the transport of energy across the shock layer by radiation. In the case of high mass missions to Mars, atmospheric density is relatively thin and supplementary braking concepts, including deployable / inflatable surfaces to increase drag or supersonic retro-propulsion need to be engaged, introducing new coupling requirements in the simulation.

The challenge of coupling is that small perturbations to shared boundary conditions across the gas - solid interface can lead to large and destabilizing perturbations in the solution of the multi-physics components. Loosely coupled algorithms involving multiple flow solver relaxation steps for every update to the material response code were the first approaches to deal with both the complexity and numerical stability in the simulations of ablation. The evolution of loosely coupled material response codes to flow solvers has been described by Chen and Milos.[1] and Kuntz et. al.[2] The Charring Material Thermal Response and Ablation Program[3] (CMA), developed by the Aerotherm Corporation in the 1960s, the Fully Implicit Ablation and Thermal Response program[4] (FIAT), developed at NASA Ames Research Center in the 1990's, and Chaleur,[5] developed at Sandia and Johnson Space Center in the 2000's, are one-dimensional material response codes. Two-dimensional material response codes, better able to handle recession at sharp corners and nose tips, have been developed more recently, including COYOTE[6–8] from Sandia National Laboratories and the Two-dimensional Implicit Thermal Response and Ablation (TITAN) Program[1] from NASA Ames. A strongly coupled algorithm with material response updates implemented at every update of the flow solver, albeit with simplifications in the gas chemistry model, is described by Conti et. al.[9] A more recent strongly coupled algorithm, including effects of micromechanical ablation, was presented by Gosse and Candler[10]

Most of these methods require use of a heat transfer coefficient and access to the thermal boundary layer edge conditions in order to specify the surface energy balance that connects the flow solver to the material

---

response.[11] See, for example, Eq. (1) in Kuntz et. al.[2] for coupling to COYOTE or Eqs. (8) and (9) in Chen and Milos[1] for coupling to TITAN. These approximations recognize that small perturbations to temperature and species concentration at the wall produce large perturbations to heating and diffusion rate. Even when line-implicit relaxation is used the abrupt change to the near wall gradients governing heating and diffusion can be destabilizing. Use of heat transfer coefficient approximations moderate these perturbations and promote convergence of the coupled systems. (Only Gosse and Candler[10] do not indicate the use of any approximations in the implementation of a surface energy balance nor do they discuss any algorithm challenges to the implementation of the interface condition.)

As noted above, simulations of aerothermal loads with ablation are evolving to strong coupling, with updates to the material response synchronized with updates to the flow solver for every relaxation step. Strong coupling provides greater opportunity to relax the solution across the interface and ultimately remove any coefficient approximations. Removing the heat transfer coefficient approximations in the surface energy balance enables a more accurate simulation - especially in situations where local geometry includes characteristic lengths that are small compared to the boundary layer thickness (e.g. cavities, gap fillers, corners). The long term goal in these topologically challenging simulations is to couple multi-dimensional material response with locally resolved flow gradients - unencumbered by any constraints to approximate heat transfer coefficients. In the process of implementing these strongly coupled algorithm changes stability problems were encountered unless very small small relaxation parameters were used that pushed the number of relaxation steps required to > 50000 for a typical, axisymmetric simulation. The purpose of this paper is to describe how modifications to the boundary condition relaxation enabled more acceptable convergence rates. Three cases are presented with large variations in blowing rates, surface temperatures, and convective and radiative heating that test the new boundary condition relaxation algorithm. Future tests are planned to engage more accurate material response on topologically complex surfaces.

II.   Nomenclature

Bold face, lowercase variable names refer to vectors. Bold face, uppercase variable names refer to matrices. Bracketed entry indicates units or quantity used to non-dimensionalize.

Roman symbols

$\mathbf{A}_{01}, \mathbf{A}_{02}$	Jacobian matrices for boundary condition updates
A_j	area of cell face j on surface
$\tilde{A}_n, \tilde{B}_n$	Fourier coefficients
c_j	mass fraction of species j
$\tilde{c}_i$	elemental mass fraction of element i
$\tilde{c}_{i,abl}$	elemental mass fraction of element i in ablation products
D_j	effective diffusion coefficient for species j
$\mathbf{F}$	transformation matrix from species continuity to elemental continuity equations
$F_{i,j}$	element of $\mathbf{F}$
$G_{j,k}$	coefficient of $\ln \rho_k$ in partial equilibrium relation for non-basis species j
h	enthalpy per unit mass
k	turbulent kinetic energy
K_j	equilibrium constant for non-base-species j
$\dot{m}$	blowing rate of ablation products per unit area
M_j	molecular weight of species j
n	normal distance to wall
$\dot{n}$	recession rate
p	pressure

q	heating rate
$\mathbf{r}_{01}, \mathbf{r}_{02}$	vector of residuals in ghost cell
t	time
x, y, z	Cartesian coordinates

Roman symbols

T	temperature
V	velocity normal to surface
V_j	diffusion velocity of species j
$\mathbf{w}_{01}, \mathbf{w}_{02}$	vector of unknowns in ghost cell

Greek symbols

α	fraction of radiation absorbed at surface
ϵ	emissivity
ε	relaxation factor
ρ	density
σ	Stefan-Boltzmann constant
χ_j	mole fraction of species j

Subscripts

0	ghost cell behind boundary
1	internal cell adjacent to boundary
c	convective
C	carbon
$cond$	conduction through surface
$char$	property of char
g	pyrolized gases
i	element index
j	species index
k	species index
rad	radiative
v	virgin material
w	wall
∞	reference condition in free stream

Superscripts

m	sub-iteration index
n	global relaxation index

III.   Conservation Equations

Program LAURA (flow solver) is used to generate all simulations presented herein. The conservation equations are provided in the literature.[12, 13] These include species conservation, momentum conservation, total energy conservation, and vibrational-electronic energy conservation if thermal non-equilibrium is modeled, and turbulence models. Park's two-temperature model is employed in the case of thermal non-equilibrium to describe modifications to the chemical kinetics. A Free Energy Minimization (FEM) algorithm is used in association with elemental species continuity equations in the case of thermochemical equilibrium modeling. In cases where radiative energy transport is included a tangent-slab approximation is used through the HARA modules that are fully-coupled within LAURA.

American Institute of Aeronautics and Astronautics

IV. Surface Boundary Conditions

Both pyrolysis and ablation are accommodated in the current analysis. Pyrolysis describes the internal decomposition of the solid which releases gaseous species into the shock layer. Ablation describes the combination of processes which consume heatshield surface material.[1] An equilibrium surface boundary condition requires that all species are equilibrated at the local wall temperature T_w with elemental mass fractions determined by the elemental continuity equation. Given a system with N_s species and N_e elements the algorithm identifies N_e base species, usually atoms, and $N_s - N_e$ non-base-species which can be created from the base set. The transformations from species continuity equations to elemental continuity equations and the definition of equilibrium constant $K_j(T)$ and stoichiometric related coefficients $G_{j,k}$ for each of the linearly independent non-base-species j shown below were derived previously.[13] The $N_s - N_e$ partial equilibrium relations for non-base species is written

$$K_j(T_w) = \sum_{k}^{species} G_{j,k} \ln \rho_k \tag{1}$$

where $\ln \rho_k$ is discretized $0.5(\ln \rho_{k,0} + \ln \rho_{k,1})$ and where subscript 0 denotes a ghost cell beneath the surface and subscript 1 denotes the cell center above the surface in the cell-centered formulation.

The integrated form of the species continuity equation[13] provides a balance for each element in which the convected elemental mass flux out of the boundary minus the diffused elemental mass flux into the boundary must equal the ablated elemental mass flux specified for the material. It is written

$$F_{i,j} \rho_j V - \tilde{c}_{i,abl} \dot{m} = F_{i,j} \left(\rho D_j \frac{\partial \chi_j}{\partial n} - c_j J_{cor} \right) \tag{2}$$

where $F_{i,j}$ is a matrix of size (N_s, N_e) that transforms species mass fraction to elemental mass fraction and V is velocity normal to the surface. Note that an effective binary diffusion coefficient is applied to model diffusive flux. A mass corrected diffusive flux[14] is also applied using $J_{cor} = \sum \rho D_j \frac{\partial \chi_j}{\partial n}$ to guarantee that the sum of diffusive flux over all species (or over all elements) goes to zero. The term $F_{i,j} \rho_j V$ is discretized $0.5(\rho_1 \tilde{c}_{i,1} V_1 + F_{i,j} \rho_{j,0} V_0)$. Other terms are evaluated as arithmetic averages or as central differences. The elemental mass fraction of ablated gas, $\tilde{c}_{i,abl}$, is a property of the thermal protection system.

In the case of no ablation the sum of Eq. 2 over all elements i is zero. These equations are not linearly independent and so the one with the largest elemental mass fraction at the cell center bordering the wall is replaced with a specification of normal momentum conservation assuming viscous terms may be ignored.

$$\frac{\partial(p + \rho V^2)}{\partial n} = 0 \tag{3}$$

A surface energy balance is written

$$-q_c - \alpha q_{rad} + \epsilon \sigma T_w^4 + q_{cond} + (\dot{m}_{char} + \dot{m}_g) h_w - \dot{m}_{char} h_{char} - \dot{m}_g h_g = 0 \tag{4}$$

In the present formulation assuming steady state ablation with the char front and virgin material front receding at the same rate, the elemental mass fractions of the pyrolysis gas, $\tilde{c}_{g,i}$, and the char, $\tilde{c}_{char,i}$ are known so that

$$\dot{n}_{char} = \frac{\dot{m}_{char}}{\rho_{char}} = \dot{n}_g = \frac{\dot{m}_g}{\rho_v - \rho_{char}} \tag{5}$$

from which it follows, using $\dot{m}_i = \dot{m}_{char,i} + \dot{m}_{g,i}$,

$$\tilde{c}_{i,abl} = \left(\frac{\rho_{char}}{\rho_v} \right) \tilde{c}_{char,i} + \left(1 - \frac{\rho_{char}}{\rho_v} \right) \tilde{c}_{g,i}. \tag{6}$$

The steady state ablation approximation also assumes that the conduction of energy into the TPS is balanced by the energy content in the gas approaching the TPS surface (minus a negligibly small energy conduction beyond the pyrolysis front) so that

$$q_{cond} = \dot{m}_{char} h_{char} + \dot{m}_g h_g \tag{7}$$

These approximations simplify the surface energy balance Eq. 4 to

$$-q_c - \alpha q_{rad} + \epsilon \sigma T_w^4 + (\dot{m}_{char} + \dot{m}_g)h_w = 0 \tag{8}$$

Note that a material response code would be required to solve for q_{cond} and $\dot{m}_g$ if a steady-state ablation approximation is not used. As will be seen subsequently, a steady-state ablation approximation over-predicts the recession rate early in the trajectory.

If there is no ablation then all surface velocities (and blowing rates) are zero. The N_s species densities are defined with $N_s - N_e$ equations for non-base-species (Eq. 1), $N_e - 1$ equations for base species through elemental conservation (Eq. 2), and one equation for normal momentum conservation (Eq. 3). Surface temperature is obtained from the surface energy balance equation (Eq. 8) which, in this case of no ablation, is simply an expression of the radiative equilibrium wall temperature approximation. Vibrational - electronic temperatures are assumed equal to translational temperature at the surface. These equations define the equilibrium surface catalytic boundary condition.

If there is ablation then an additional boundary condition is needed to define $\dot{m}_{char}$. (Note that $\dot{m}_g$ is obtained from the steady-state ablation approximation (Eq. 5, 7) or from a material response code. Also note that the char density ρ_{char} and the virgin material density ρ_v are assumed known properties of a charring ablator.) The closing relation recognizes that the solid surface char participates as a reaction partner with the gas. It is implicitly assumed here that a single equilibrium relation between gaseous carbon and solid carbon in the char is sufficient to define $\dot{m}_{char}$, regardless of the presence of any other elements in the char. More comprehensive models of material response[15] dealing with this (and other) simplifications have not been tested here. Therefore, the closing relation to define $\dot{m}_{char}$ is expressed

$$\rho_{C,w} = \mathrm{M}_C K_{char,C}(T_w) \tag{9}$$

A curve fit of the equilibrium constant $K_{char,C}$ is expressed

$$K_{char,C} = 1.238\,10^{11}T^{-1.487}\exp\left(\frac{-87110.4}{T}\right) \tag{10}$$

Note that this closing relation has only implicit dependence on $\dot{m}_{char}$; the blowing rate is adjusted until the equilibrium condition is attained at a wall temperature that satisfies the surface energy balance.

A.   Implementation of Boundary Conditions

It is observed that the mutual sensitivity of dT_w, $d\dot{m}$, and $d\ln\rho_{C,0}$ changes with increasing surface temperature - likely due to diffusion limited presence of oxygen near the wall as blowing rates increase. A surface temperature switch T_{sw} is defined to enable convergence. Three conditions with equilibrium surface chemistry are considered: (1) no ablation; (2) ablation with $T_w \leq T_{sw}$; and (3) ablation with $T_w > T_{sw}$. T_{sw} is a temperature that defines where the implementation algorithm is switched. Numerical experiments indicate $T_{sw} = 2800$K. The boundary conditions at ghost cells are updated in parallel with the interior cells at every relaxation step n. As will be shown below, when $T_w > T_{sw}$ the expected atomic carbon mass fraction c_C at the surface starts to rise above a trace level and so the value of c_C from the current interior relaxation step can be used to update the surface temperature for the next relaxation step. When $T_w < T_{sw}$ the expected $\dot{m}$ is small, and the linearized set of boundary conditions, including the implicit dependence of $\dot{m}$ on the species densities, can be solved using a strongly coupled Newton relaxation.

Note that in this solution procedure the convective heating and diffusion of species to the surface are calculated directly from the local gradients. There is no approximation involving film cooling coefficients. The drawback of this approach is that small changes in boundary values can lead to large, physically unrealistic changes in the convective heating rates and diffusion rates. The off-body points take longer to respond in the global solution. The use of line relaxation and relaxation factors on boundary updates enable convergence on the order of 20,000 to 40,000 global relaxation steps, including re-gridding and shock alignment for the evolving solution.

1. No Ablation

In the case of no ablation the ghost cell unknowns include species densities and temperature. All other quantities are explicitly formulated from these unknowns. Temperature is first computed from Eq. 8 as

$$T_w^{n+1} = \varepsilon \left(\frac{q_c^n + \alpha q_{rad}^n}{\epsilon \sigma} \right)^{1/4} + (1 - \varepsilon) T_w^n \tag{11}$$

with relaxation factor $\varepsilon = 0.001$. Densities are computed by the simultaneous solution of Eqs. 1, 2, and 3 for $\ln \rho_{j,0}$ with surface ablation rates and normal velocity set to zero. A sub-iteration over index m of these equations with a Newton method is employed to a residual convergence of $1x10^{-10}$.

$$\mathbf{A}_{01}^m \Delta \mathbf{w}_{01} = \mathbf{r}_{01}^m \tag{12}$$

Here $\Delta \mathbf{w}_{01} = \left(\mathbf{w}_{01}^{m+1} - \mathbf{w}_{01}^m \right)$ is a vector of N_s unknowns equal to $\ln \rho_{j,0}$. $\mathbf{r}_{01}$ is the vector of residuals of Eqs. 1, 2, and 3 evaluated at T_w^{n+1} and $\mathbf{A}_{01}$ is the Jacobian of $\mathbf{r}_{01}$ with respect to $\mathbf{w}_{01}$. The sub-iteration updates are applied with a solution dependent relaxation factor $\eta_j = m/(\Delta w_{j,01}^2 + 2m)$.

$$w_{j,01}^{m+1} = w_{j,01}^m + \eta_j \Delta w_{j,01} \tag{13}$$

At the beginning of the sub-iterations $m = 1$ we initialize $\mathbf{w}_{01}$ with the average value of $\ln \rho_j$ at the cell centers bounding the surface. This initialization and use of relaxation factors η_j are designed to accommodate difficult transients as the global solution evolves. If sub-iterations fail to converge after 300 steps a warning is printed but the global solution is allowed to continue. It is not uncommon to see such warnings early in the evolution of the simulation but full convergence at all surface nodes is achieved as the global solution converges.

2. Ablation with $T_w \leq T_{sw}$

There is one extra unknown, $\dot{m}$, when ablation is engaged. In contrast to the previous implementation the wall temperature in this case is computed after the coupled solution of Eqs. 1, 2, 3, and 9.

$$\mathbf{A}_{02}^m \Delta \mathbf{w}_{02} = \mathbf{r}_{02}^m \tag{14}$$

$\mathbf{r}_{02}^m$ is the same as $\mathbf{r}_{01}$ but with the addition of one extra element equal to the residual of Eq. 9. In like manner, $\mathbf{w}_{02}$ is the same as $\mathbf{w}_{01}$ but with the addition of one extra unknown $\dot{m}$. $\mathbf{A}_{02}^m$ is the Jacobian of $\mathbf{r}_{02}$ with respect to $\mathbf{w}_{02}$. The sub-iterations are engaged exactly as defined in the previous section so that

$$w_{j,02}^{m+1} = w_{j,02}^m + \eta_j \Delta w_{j,02} \qquad 1 \leq j \leq N_s \tag{15}$$

$$w_{j,02}^{m+1} = w_{j,02}^m + \Delta w_{j,02} \qquad j = N_s + 1 \tag{16}$$

There is no additional relaxation factor required on $\dot{m}$ for the sub-iterations to converge. However, at the conclusion of the sub-iterations we take a fraction of the updated blowing rate.

$$\dot{m}^{n+1} = \varepsilon \Delta w_{(N_s+1),02} + \dot{m}^n \tag{17}$$

The temperature is next updated using Eq. 8.

$$T_w^{n+1} = \varepsilon \left(\frac{q_c^n + \alpha q_{rad}^n - \dot{m}^{n+1} h_w^n}{\epsilon \sigma} \right)^{1/4} + (1 - \varepsilon) T_w^n \tag{18}$$

3. Ablation with $T_w > T_{sw}$

In this case T_w is computed from the requirement of chemical equilibrium with the surface using Eq. 9.

$$K_{char,C}(T_w^m) = \frac{\left(\rho_{C,0}^n \rho_{C,1}^n \right)^{1/2}}{\mathrm{M}_C} \tag{19}$$

American Institute of Aeronautics and Astronautics

A sub-iteration over index m on this equation is executed using a Newton method until convergence is achieved. A fraction of this updated value is applied to advance the surface temperature.

$$T_w^{n+1} = T_w^n + \varepsilon(T_w^m - T_w^n) \tag{20}$$

Densities are computed by the simultaneous solution of Eqs. 1, 2, and 3 for $\ln \rho_{j,0}$ with $T_w = T_w^{n+1}$ and $\dot{m} = \dot{m}^n$ using the algorithm described previously in Eqs. 12 and 13. Finally, $\dot{m}^{n+1}$ is computed from the surface energy balance Eq. 8.

$$\dot{m}^{n+1} = \varepsilon \frac{\left(q_c^n + \alpha q_{rad}^n - \epsilon\sigma(T_w^{n+1})^4\right)}{h_w^{n+1}} + (1-\varepsilon)\dot{m}^n \tag{21}$$

B. Implementation of Surface Recession: Shape Change and Grid Adaptation

1. Charring Ablator

The charring ablator model defines mass loss in two ways. (Mechanical erosion is ignored.) As heat is conducted into virgin material a component of the material, usually a resin, undergoes decomposition through pyrolysis. If the back side of the TPS is sealed, pyrolysed gases escape into the shock layer through the remaining char. It is assumed that the original contour of the TPS is preserved until the char itself, predominantly carbon, begins to sublimate - a process that requires higher temperatures then pyrolysis. Changes to the outer mold line between two trajectory points are therefore a function of the char mass loss rate, $\dot{m}_{char}$, the char density ρ_{char} and the time between trajectory points, Δt.

$$\Delta n = \frac{\dot{m}_{char}\Delta t}{\rho_{char}} = \frac{\rho_{char}}{\rho_v}\frac{\dot{m}_i}{\rho_{char}}\Delta t = \frac{\dot{m}}{\rho_v}\Delta t \tag{22}$$

The last equalities are enabled by the steady-state ablation approximation of Eq. 5.

2. Non-charring Ablator

In this model, only a single component ablation process is considered without any identifiable char remaining as surface recession proceeds. In the model setup, it is convenient to define a "char" density, ρ_{char} equal to the virgin TPS density, ρ_v. Consequently, "char" refers to the receding material which, in this case, is identical to the virgin material. Therefore, from Eq. 5 we note that $\dot{m}_g = 0$ and therefore

$$\Delta n = \frac{\dot{m}_{char}\Delta t}{\rho_{char}} = \frac{\dot{m}}{\rho_{char}}\Delta t = \frac{\dot{m}}{\rho_v}\Delta t \tag{23}$$

This result is equivalent to the expression for the charring ablator with the additional simplification that $\rho_{char}/\rho_v = 1$.

3. Explicit Shape Change

Blowing rates $\dot{m}_{i,j}$ are evaluated at cell wall i,j in the cell-centered, finite-volume LAURA code. The displacement at node $(i+1/2, j+1/2)$ is evaluated as the average of surrounding surfaces using the converged solution for trajectory point nt.

$$\Delta n_{i+1/2,j+1/2}^{nt} = \frac{t^{nt+1} - t^{nt}}{4\rho_v}\left(\dot{m}_{i,j}^{nt} + \dot{m}_{i+1,j}^{nt} + \dot{m}_{i,j+1}^{nt} + \dot{m}_{i+1,j+1}^{nt}\right) \tag{24}$$

The displacement components at this node are computed from the cross-product of the diagonals defined by the surrounding cells.

$$
\begin{aligned}
d\vec{r}_{1,i+1/2,j+1/2}^{nt} &= \vec{r}_{i+3/2,j-1/2}^{nt} - \vec{r}_{i-1/2,j+3/2}^{nt} & (25)\\
d\vec{r}_{2,i+1/2,j+1/2}^{nt} &= \vec{r}_{i+3/2,j+1/2}^{nt} - \vec{r}_{i-1/2,j-1/2}^{nt} & (26)\\
\vec{n}_{i+1/2,j+1/2}^{nt} &= d\vec{r}_{1,i+1/2,j+1/2}^{nt} \times d\vec{r}_{2,i+1/2,j+1/2}^{nt} / |d\vec{r}_{1,i+1/2,j+1/2}^{nt} \times d\vec{r}_{2,i+1/2,j+1/2}^{nt}| & (27)\\
\Delta\vec{r}_{i+1/2,j+1/2}^{nt} &= \Delta n_{i+1/2,j+1/2}^{nt}\vec{n}_{i+1/2,j+1/2} & (28)
\end{aligned}
$$

The volume grid for the new solution at time t^{nt+1} is now computed as

$$\vec{r}^{\,nt+1}_{i+1/2,j+1/2,k+1/2} = \vec{r}^{\,nt}_{i+1/2,j+1/2,k+1/2} + \Delta \vec{r}^{\,nt}_{i+1/2,j+1/2} \tag{29}$$

where each volume node is displaced according to its corresponding surface node in this structured grid formulation. In the case of axi-symmetric geometries displacements are computed along the original bounding planes defining the symmetry boundaries.

Explicit shape change formulations are known to be subject to numerical instabilities that can induce oscillations in surface contours and heating.[2] These problems are most robustly dealt with through the use of a sub-iterative procedure that computes the shape at time $nt+1$ as a function of the simulated solution at time $nt+1$.[2] Root causes of the explicit stability limit are explored in the Appendix and a filtering algorithm is introduced that enhances explicit stability. The baseline explicit update described above is referenced as a two-cell stencil algorithm. The enhanced explicit update described in the Appendix is referenced as a four-cell stencil algorithm.

4. Volume Grid Adaptation

All simulations incorporate grid adaptation as an integral part of the flow solver. The outer boundary of the grid is aligned with the captured shock. The near wall resolution requires $0.1 \leq \frac{\rho c \Delta n}{\mu} \leq 1$. In cases with shape change, the volume grid is re-adapted every 500 relaxation steps for the first 5000 iterations giving a total of 10 adaptations per trajectory point.

V. Simulations

All of the flow field simulations presented here, including fully coupled radiation and ablation, are executed with programs LAURA[16] and HARA.[17] The test cases span conditions for which peak mass loss rate ranges from 0.06 kg/m²-s to 140 kg/m²-s. Line implicit relaxation is applied for all solutions.

A. IRV-2

The IRV-2 geometry is described in the references.[2] The IRV-2 vehicle is a sphere-biconic-cylinder with a nose radius of 0.01905 m and total length of 1.386 m. The biconic angles are 8.42 deg. and 6.10 deg. The fore-cone breaks at 0.1488 m which marks the extent of the present simulations. Free stream conditions across the trajectory are defined in Table 1. A trajectory data file enables LAURA to sequentially compute a flow field at a trajectory point, compute a shape change based on the $\dot{m}$ distribution, re-grid, and move on to the next trajectory point. The baseline grid uses 64 cells normal to the body and 64 cells around the body with 30 of those cells on the nosetip. The outer boundary is aligned with the captured bow shock. The cell Reynolds number at the wall is set to 1.0. A grid convergence test (double the grid density across the shock layer) at trajectory point 16 indicates stagnation point heating converged to 0.75%. Nineteen species for products of high temperature air and products from a carbon ablator include: N, O, N_2, O_2, NO, N^+, O^+, N_2^+, O_2^+, NO^+, e^-, C, C_2, C_3, C_4, C_5, CO, CN, CO_2. Laminar flow in thermochemical nonequilibrium is specified for the first 15 trajectory points. Thermal equilibrium is specified for trajectory point 16 and beyond. These specifications are consistent with the original refernce.[2] Two thermal protection system (TPS) densities are simulated for this trajectory: a low-density carbon ($\rho_v = 544.63$ kg/m³) and carbon-carbon ($\rho_v = 1800$ kg/m³). The low-density tests induce larger recessions for equivalent blowing rates and provide greater opportunity to explore stability of the shape change algorithm. Carbon-carbon is the material specified for the IRV-2 test.

1. Low-Density TPS

Results of simulations for the first six trajectory points are presented in Fig. 1 for the low-density TPS. Mass loss rate $\dot{m}$ is shown in cyan, the atomic carbon mass fraction c_C is shown in green, the surface temperature is shown in blue, convective heating is shown in red, and body shape is shown in black as a function of time during first 11.5 seconds of IRV-2 test. The axes are defined to provide an aspect ratio of approximately one for the body shape (black line). The body shape is presented nose down. Recession of the stagnation point with time can be read as the point where the black line intersects the left axis. The carbon mass fraction is

tracked because its equilibration with the solid carbon on the surface is a key element of closing the surface boundary condition.

<div align="center">

Table 1. Free Stream Conditions for IRV-2[2]

Traj- Point	Time (s)	Altitude (m)	Velocity (m/s)	Temp. (K)	Pressure (Pa)	Density (kg/m^3)	Mach No.	Thermal State
1	0	66935	6780.6	227.81	8.1757	1.2505×10^{-4}	22.41	TNEQ[a]
2	4.25	55842	6788.3	258.02	37.362	5.0454×10^{-4}	21.08	TNEQ
3	6.75	49290	6785.2	270.65	88.118	1.1344×10^{-3}	20.57	TNEQ
4	8.75	44042	6773.0	261.40	169.50	2.2593×10^{-3}	20.90	TNEQ
5	10.25	40108	6752.4	250.35	287.14	3.9957×10^{-3}	21.29	TNEQ
6	11.50	36836	6722.0	241.50	445.52	6.4268×10^{-3}	21.58	TNEQ
7	12.50	34229	6684.3	234.30	644.52	9.5832×10^{-3}	21.78	TNEQ
8	13.25	32283	6644.9	228.76	863.14	1.3145×10^{-2}	21.91	TNEQ
9	13.95	30480	6596.7	226.91	1127.6	1.7313×10^{-2}	21.84	TNEQ
10	14.75	28236	6527.1	224.73	1568.1	2.4310×10^{-2}	21.71	TNEQ
11	15.50	25772	6428.3	222.35	2256.0	3.5348×10^{-2}	21.50	TNEQ
12	16.25	22949	6286.6	219.47	3520.8	5.5888×10^{-2}	21.17	TNEQ
13	17.00	19790	6091.7	216.65	5705.3	9.1741×10^{-2}	20.64	TNEQ
14	17.75	16355	5836.4	216.65	9723.1	1.5635×10^{-1}	19.77	TNEQ
15	18.25	13962	5631.8	216.65	14170	2.2786×10^{-1}	19.08	TNEQ
16	18.50	12748	5519.6	216.65	17379	2.7946×10^{-1}	18.70	TEQ[b]
17	18.75	11528	5401.2	216.65	20984	3.3743×10^{-1}	18.30	TEQ
18	19.00	10309	5277.1	221.31	25309	3.9840×10^{-1}	17.69	TEQ
19	19.50	7892	5014.3	236.86	36168	5.3196×10^{-1}	16.25	TEQ
20	20.00	5536	4736.5	252.11	50198	6.9366×10^{-1}	14.88	TEQ
21	20.50	3273	4449.6	267.04	67922	8.8610×10^{-1}	13.58	TEQ
22	21.00	1129	4159.7	280.68	88253	1.0954×10^{0}	12.38	TEQ
23	21.28	0	4000.0	288.15	101325	1.2250×10^{0}	11.75	TEQ

</div>

[a] thermal nonequilibrium, [b] thermal equilibrium

Fig. 2 compares simulation results at trajectory points 7, 9, and 11 using the baseline, 2-cell stencil, explicit shape change algorithm (Eqs. 24 - 27) with the 4-cell stencil algorithm (Eq. 32 defined in the Appendix). The two-cell stencil results are on the left and the four-cell stencil on the right for a given trajectory point. Oscillations in heating and blowing rate are significantly larger for the baseline algorithm. Oscillations in body shape are present but are difficult to see except at the 15.5 s point for the baseline algorithm. The correlation of heating spikes with local surface compressions is more evident in Fig. 3. This figure shows the evolution of the node shape (black) and heating (red) over the first eleven trajectory points with the low-density (TPS). Very slight surface waves produce a relatively large perturbation in surface heating, blowing rate, and atomic Carbon mass fraction. Surface temperature is relatively insensitive to these perturbations. Averaging over a larger stencil inhibits the growth of instability but does not eliminate it. In essence, a larger effective Δx yields a larger allowable Δt as discussed in the Appendix.

2. Carbon-carbon TPS

Results of simulations for odd number trajectory points using the carbon-carbon TPS are presented in Fig. 4. Note that the first three subfigures use a different range than the last nine subfigures. Shape change for these cases used the 4-cell stencil algorithm. Note that the mass loss rate $\dot{m}$ at a given trajectory point for the high-density TPS (Fig. 4 d, e, f) is approximately equal to the mass loss rate for the low-density TPS (Fig. 2). Even though the evolution of $\dot{m}$ is equivalent up to trajectory point 11 at 15.5 s for the two TPS
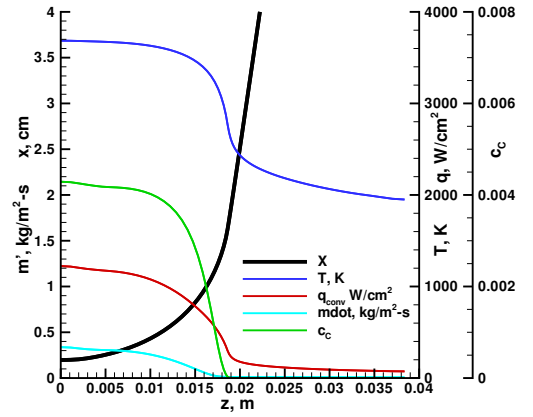
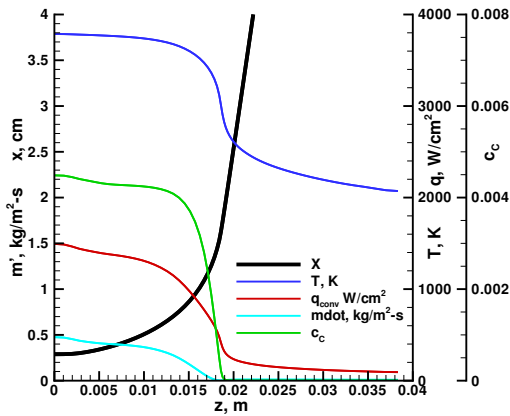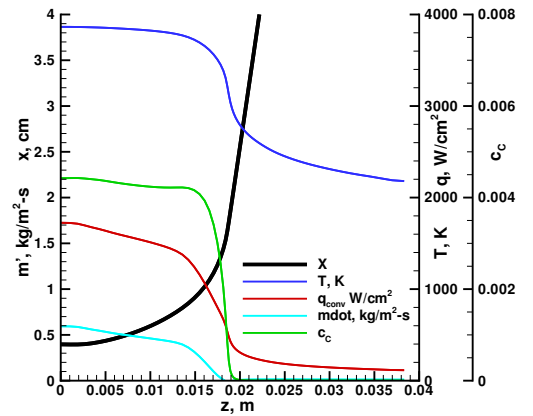American Institute of Aeronautics and Astronautics
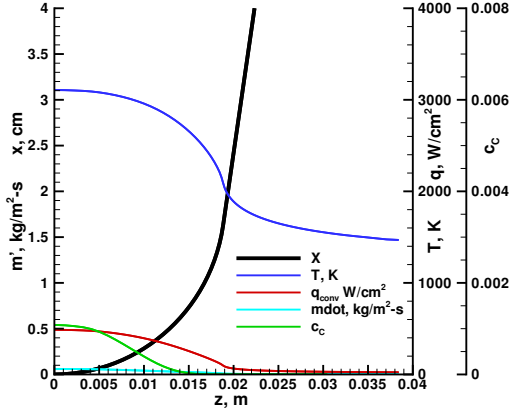
(a) t = 0 s
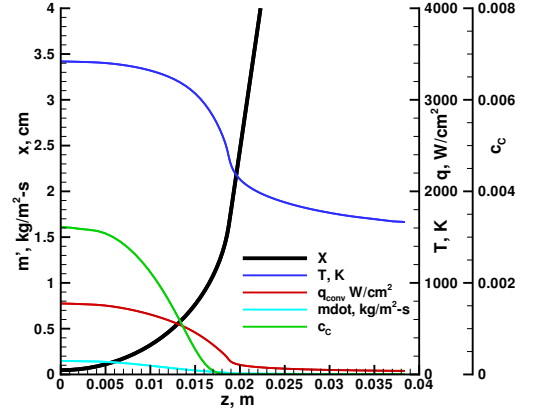
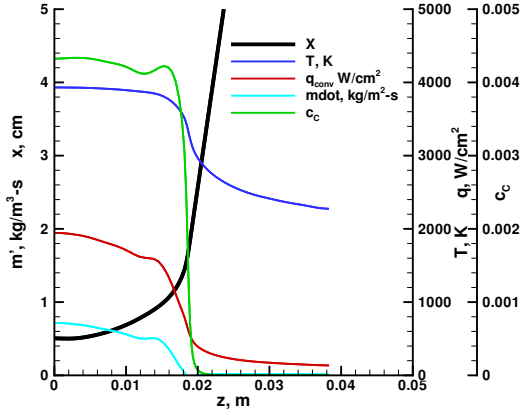(b) t = 4.25 s
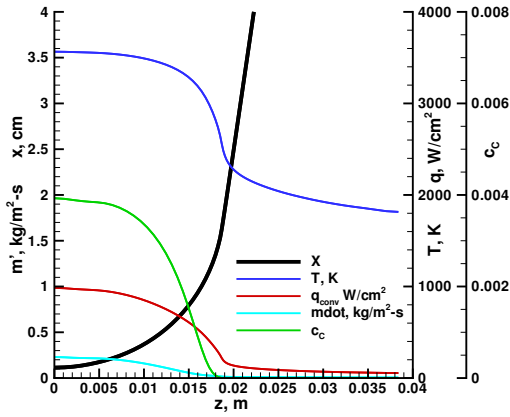
(c) t = 6.75 s

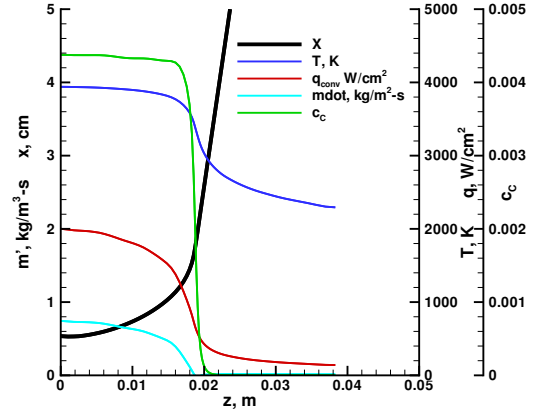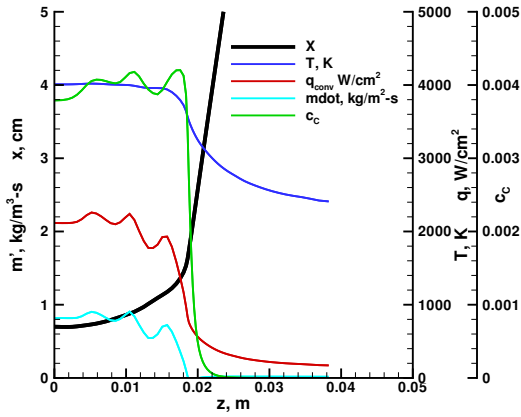(d) t = 8.75 s

(e) t = 10.25 s

(f) t = 11.50 s

Figure 1. **Mass loss rate $\dot{m}$ (cyan), atomic carbon mass fraction c_C (green), surface temperature (blue), convective heating (red), and body shape (black) as function of time during first 11.5 seconds of IRV-2 low density char test.**
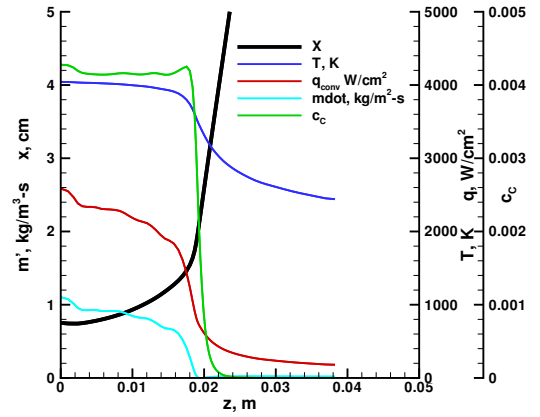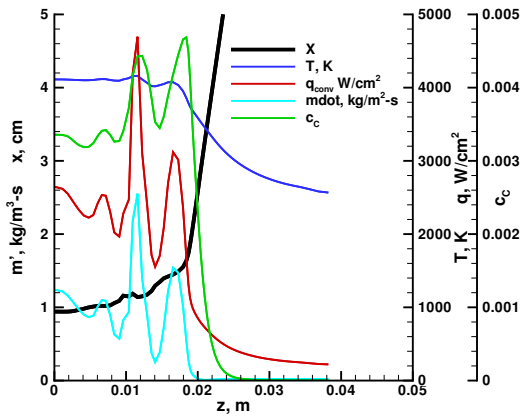
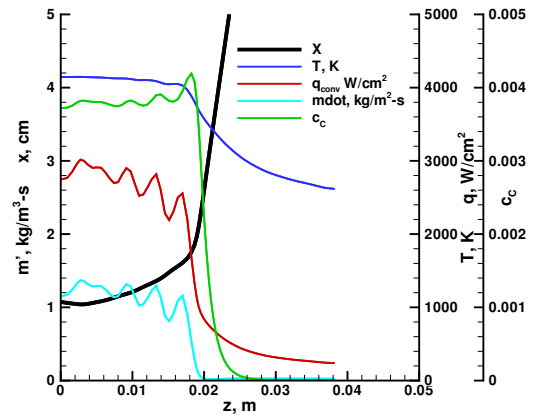(a) t = 12.5 s, 2-cell stencil

(b) t = 12.5 s, 4-cell stencil

(c) t = 13.95 s, 2-cell stencil

(d) t = 13.95 s, 4-cell stencil

(e) t = 15.5 s, 2-cell stencil

(f) t = 15.5 s, 4-cell stencil

Figure 2. **Mass loss rate** $\dot{m}$ **(cyan), atomic carbon mass fraction** c_C **(green), surface temperature (blue), convective heating (red), and body shape (black) as function of time for** $12.5 \leq t \leq 15.5$ **IRV-2, low-density TPS. Slight irregularities in the body shape cause large oscillations in heating that are moderated through use of a filtering algorithm extending over a larger stencil.**

(a) 2-cell stencil

(b) 4-cell stencil
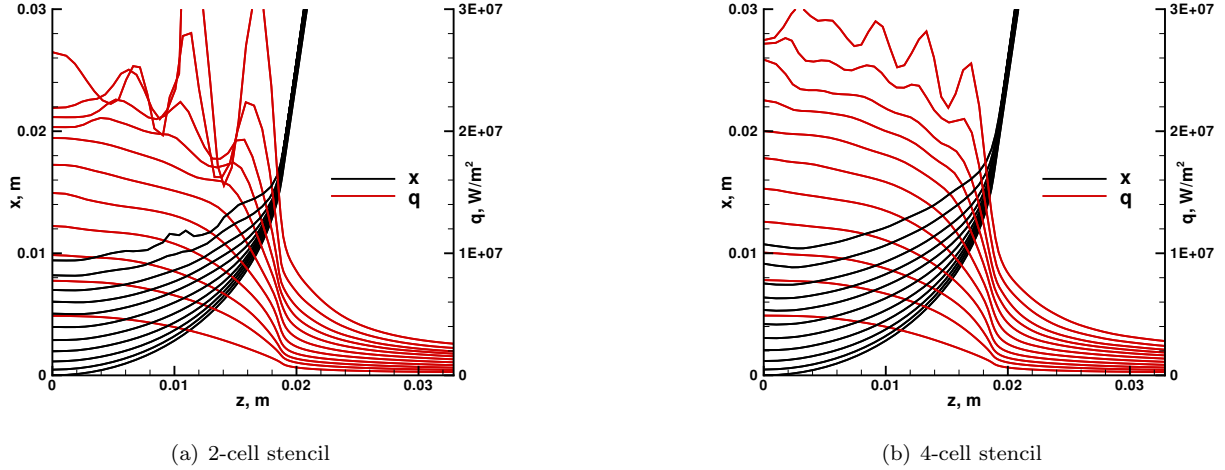
Figure 3. Evolution of body shape and heating distribution for first 11 simulation points spanning $0 \leq t \leq 15.5s$ with low-density TPS.

systems one observes that the high-density TPS shows no sign of a shape change induced instability (Fig. 4(f)) whereas the the low-density TPS case shows onset of the instabilities at this same point (Fig. 2(f)). This behavior indicates that the shape change instability is associated with the recession rate distribution as opposed to mass loss rate distribution. Some weak oscillations in the heating and blowing rate are evident at trajectory point 17 (18.75 s, Fig. 4(i)). These oscillations grow slowly through trajectory point 19 ($t = 19.5$ s, Fig. 4(j)). Significant oscillations first appear at trajectory point 20 (not shown) and continue to trajectory point 23 (Fig. 4(l)).

A key result of Fig. 4 is that it demonstrates that boundary condition implementation is robust for a wide range of conditions. Temperature and heating rate vary from 1472 K and 24 W/cm^2 at the trailing edge for trajectory point 1 to 4450 K and 5000 W/cm^2 at the stagnation point for trajectory point 17. Trajectory points 1-13 have the switch temperature $T_{sw} = 2800$K included in the domain. In these cases, different relaxation sequences are used to compute the boundary conditions.

The convergence history for this sequence of cases is presented in Fig. 5. Trajectory point 1 had been computed previously. Trajectory points 2 - 15 (Fig. 5(a)) were run assuming thermal non-equilibrium. Trajectory points 16 - 23 (Fig. 5(b)) were run assuming thermal equilibrium. The cases are automatically sequenced using a trajectory data file. A detail of the convergence history for trajectory points 8 and 9 is presented in Fig. 5 c. A spike in the error norm is evident after sequencing to the next trajectory point. Ten additional spikes associated with grid adaptation every 500 relaxation steps are also recorded. There is a nearly monotone decrease in error norm after the last grid adaptation until a convergence criteria of 3 10^{-10} is achieved. (The final two trajectory points show the error norm reduction stalls - probably associated with the growing shape change instabilities.) The non-monotone spikes at approximately 39500 s and 44000 s are associated with a change of temperature across T_{sw} late in the convergence process causing an abrupt change in the relaxation of the boundary condition. (The boundary conditions do not change - only the relaxation process to satisfy the boundary conditions change.) Still, one can see in the detailed Fig. 6 that all surface quantities are smoothly resolved across $T_{sw} = 2800$K at convergence. Note that c_C rapidly goes to trace levels at $T = 2800$K and that $\dot{m}$ remains at a small, nearly constant level for $T_w < 2800$K.

At trajectory points 6-9 a negative value of $\dot{m}$ is computed in regions just behind the blunt nose. Surface pressure and temperature tend to rapidly decrease in these regions. A significant amount of ablated species are carried to these points from upstream locations. Carbon may condense on the surface (negative $\dot{m}$) in order to equilibrate the atomic carbon vapor pressure.[18]

Stagnation point results are compared to a reference calculation by Kuntz, et. al.[2] in Fig. 7. The LAURA results in red with diamond symbols are overlayed on the original figures pulled from the reference. The relevant reference curves are indicated by solid black lines with filled square symbols indicating their
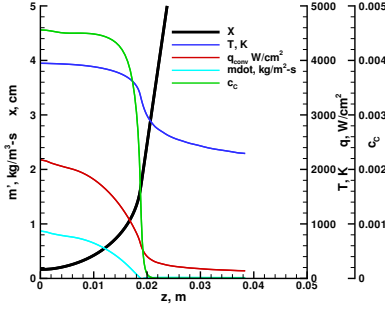
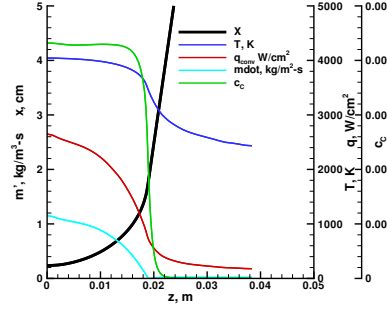American Institute of Aeronautics and Astronautics
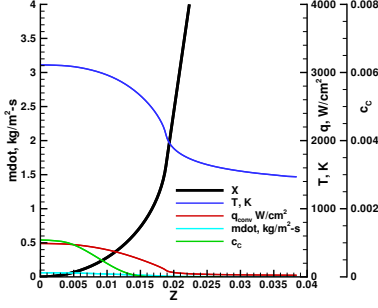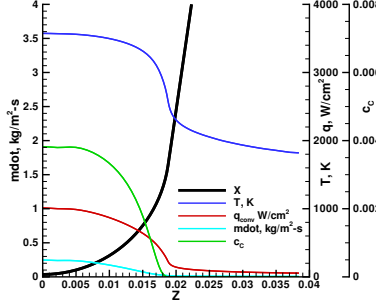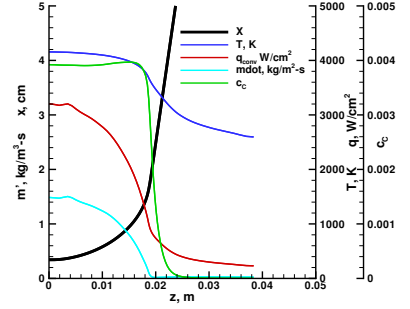
(a) t = 0.00 s, point 1
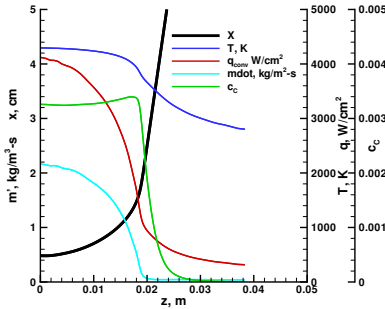
(b) t = 6.75 s, point 3
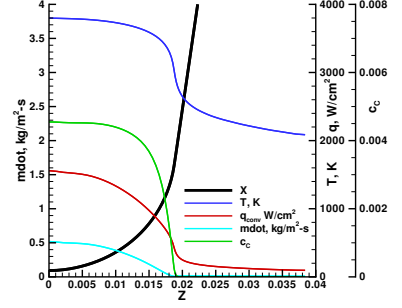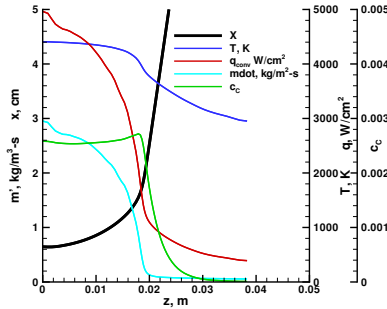
(c) t = 10.25 s, point 5
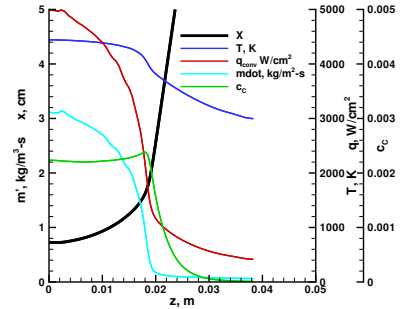
(d) t = 12.50 s, point 7

(e) t = 13.95 s, point 9

(f) t = 15.50 s, point 11
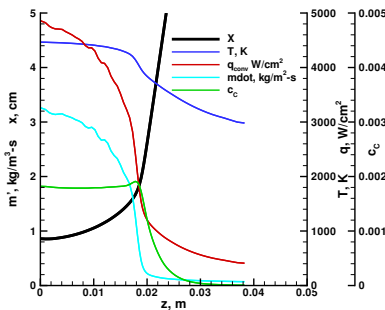
(g) t = 17.00 s, point 13
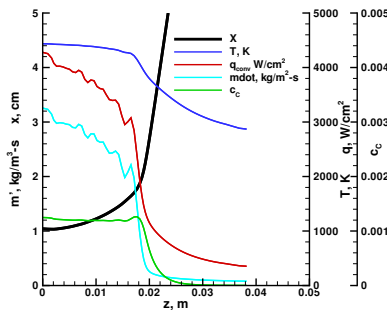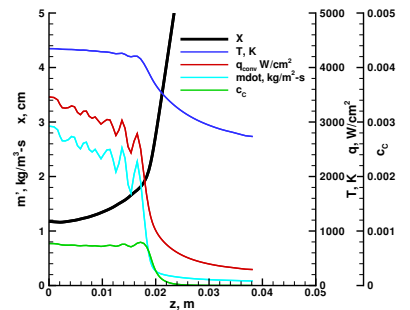
(h) t = 18.25 s, point 15

(i) t = 18.75 s, point 17
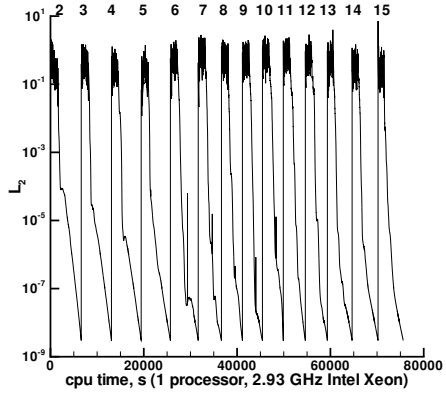
(j) t = 19.50 s, point 19
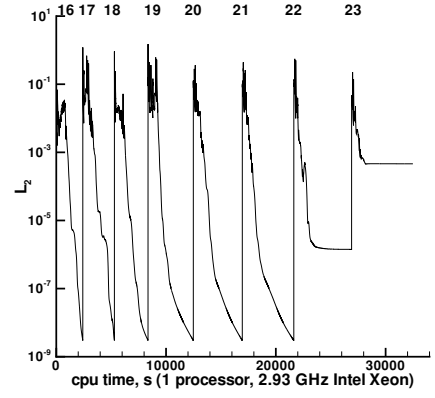
(k) t = 20.50 s, point 21
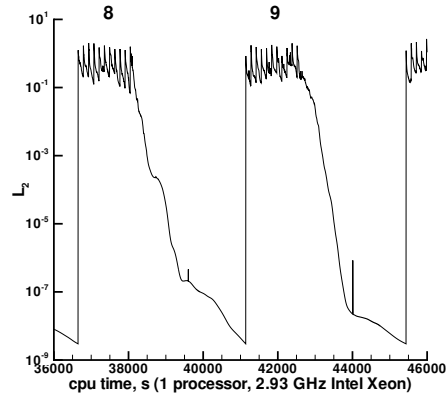
(l) t = 21.28 s, point 23

Figure 4. **Mass loss rate $\dot{m}$ (cyan), atomic Carbon mass fraction c_C (green), surface temperature (blue), convective heating (red), and body shape (black) as function of time for carbon-carbon TPS.**

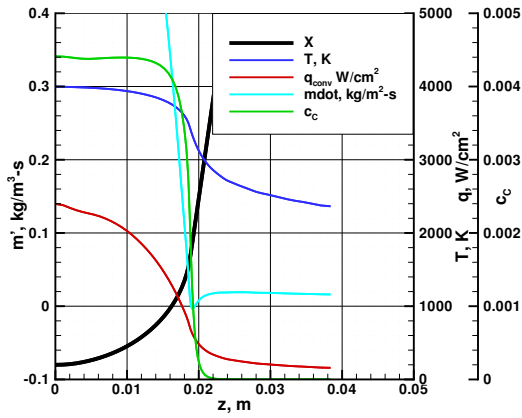(a) trajectory points 2 - 15, TNEQ

(b) trajectory points 16 - 23, TEQ
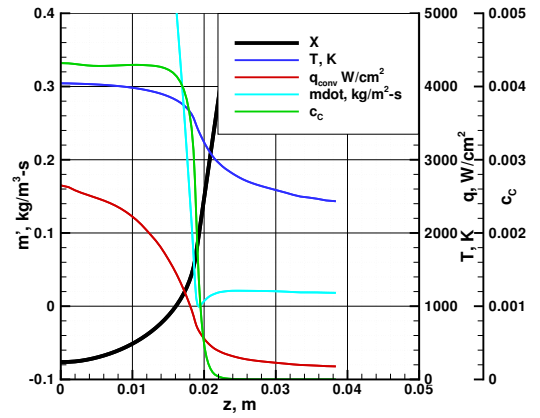

(c) trajectory points 8 and 9

**Figure 5. Convergence history.**

(a) t = 13.25 s, point 8

(b) t = 13.95 s, point 9

Figure 6. Detail of boundary condition distributions highlighting behavior across $T_w = T_{sw} = 2800$K.

iterative algorithm. Solid black circles indicate results from the engineering code ASCC[19] used by Kuntz et. al. as another reference calculation. The reference calculation, SACCARA, used a material response code, COYOTE, with initial conditions corresponding to a cold, non-ablating wall. The LAURA simulation replaces the material response code with the steady state ablation approximation - a simpler but less accurate model of the true evolution of heat transfer through the TPS and subsequent mass loss. Note that an earlier LAURA simulation[20] of this case did show good agreement with the early material response. That simulation coupled a one-dimensional material response code and was not used here because it implicitly incorporates approximations that bypass the boundary condition relaxation strategy tested here.

The LAURA surface temperature starts at a very high temperature because the body is initialized at time $t = 0$ as if it had already achieved a steady state ablation condition. (Fig. 7(b)) It takes the more accurate material response simulation approximately 10 seconds before the surface temperature asymptotes to the level predicted by the steady state ablation approximation. The surface temperature is computed from Eq. 9 requiring equilibration of atomic carbon with surface char.

The LAURA heating rate starts 17% lower than the SACCARA value at $t = 0$ but after 10 seconds begins to rise above the reference calculation. (Fig. 7(a)) This difference is again associated with the LAURA initial condition that has a fully established blowing rate and larger surface temperature at $t = 0$ as compared to the reference. Peak heating occurs near $t = 19s$ for both LAURA and SACCARA with LAURA approximately 20% larger than the reference value. The blowing rate predicted by LAURA is larger than that predicted by SACCARA/COYOTE up to the onset of peak heating at approximately $t = 18s$. (Fig. 7(c)) It is likely that the steady state ablation approximation is still too aggressive during this period and the conduction energy flux into the TPS is not yet balanced by the energy flux in the outgassing. The higher heating rates in LAURA compared to SACCARA beyond $t = 12s$ are more difficult to explain. While there has been more surface recession in LAURA at a given time the body shape appears to be slightly blunter than SACCARA predicts so effective radius is not a satisfactory explanation. Both simulations compute an equilibrium species mass fraction at the surface. A grid convergence test at trajectory point 16 using 128 cells across the shock layer produced a 0.76% reduction in heating - not nearly enough to account for current differences. LAURA was run with ionization but the mass fraction of NO^+ in the stagnation region is only 0.0004. At present it is thought that the conduction terms and energy storage terms ignored in the steady state ablation approximation remain sufficiently large compared to energy exiting the surface through sublimation for this simulation.
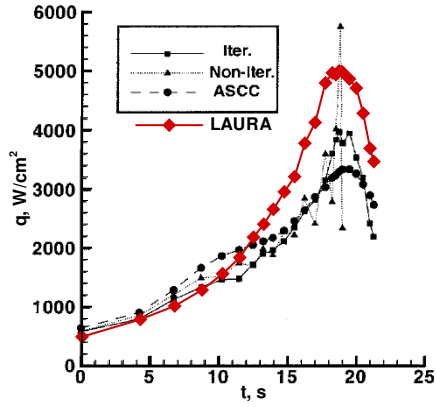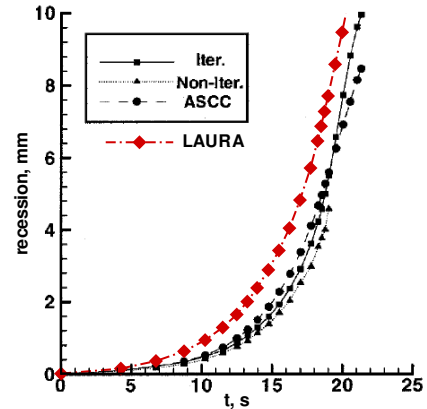
(a) heating
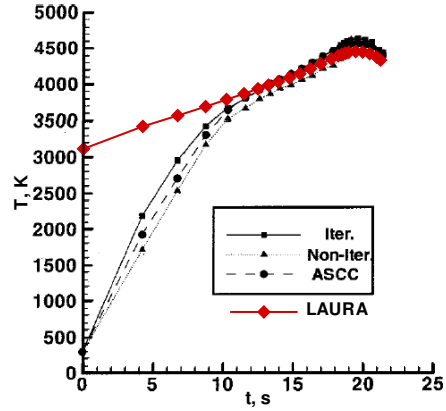
(b) surface temperature
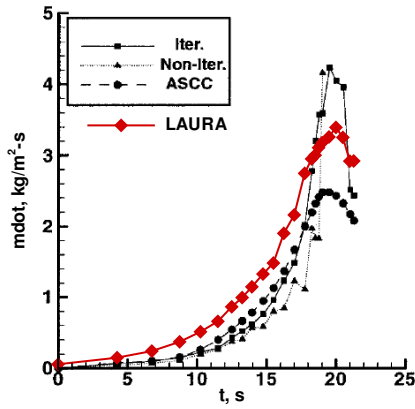
(c) mass loss rate

(d) recession

Figure 7. Stagnation point heat flux, temperature, blowing rate, and recession. Black lines taken from Kuntz, et. al.[2] for material response using COYOTE coupled with the SACCARA flow solver. Red lines are for LAURA using quasi-steady, equilibrium ablation model.

B. Galileo Probe

The Galileo probe entered the Jovian atmosphere at a relative velocity of 47.4 km/s in December, 1995.[21] The vehicle forebody shape is a 44.86 deg. spherically capped cone with nose radius 22.2 cm and base radius of 63.2 cm. Free stream conditions for the current simulation are: $V_\infty = 41591$ m/s, $\rho_\infty = 3.49x10^{-4}$ kg/m^3, and $T_\infty = 300$. K. The flow field is resolved with 52 cells around the body and 100 cells across the shock layer. Sixteen species for products of high temperature hydrogen-helium atmosphere and ablation products include: H_2, H, H^+, He, He^+, e^-, C, C^+, CO, C_2, C_3, C_2H, O, O^+, C_5, CO_2. The elemental mass fractions of a charring ablator are specified: $\tilde{c}_C = 0.92$, $\tilde{c}_H = 0.02$, and $\tilde{c}_O = 0.06$. The free stream atmospheric composition is specified $c_{H_2} = 0.76056$ and $c_{He} = 0.23944$. The shock layer is assumed to be in chemical equilibrium using the free-energy-minimization option in LAURA. The Cebeci-Smith algebraic turbulence model is applied. Radiation is fully coupled with the solution of the shock layer.

Figure 8 presents distributions of mass loss rate $\dot{m}$ in cyan, the atomic Carbon mass fraction c_C in green, the surface temperature in blue, convective heating in red, and radiative heating in violet. The radiative heating is much larger than convective in this case. Peak mass loss rate exceeds 7 kg/m^2-s. The surface temperature is nearly flat at approximately 4000 K. The solid line indicates use of a film coefficient approximation which is in excellent agreement with the new boundary condition implementation shown by dashed lines.

The large blowing rates driven by radiative heating essentially displace the boundary layer off the body. The extent of this displacement is evident in Fig. 9(a) which shows the carbon mass fraction in the blown gas layer and in Fig. 9(b) which shows the ionized atomic hydrogen in the radiating, inviscid layer.
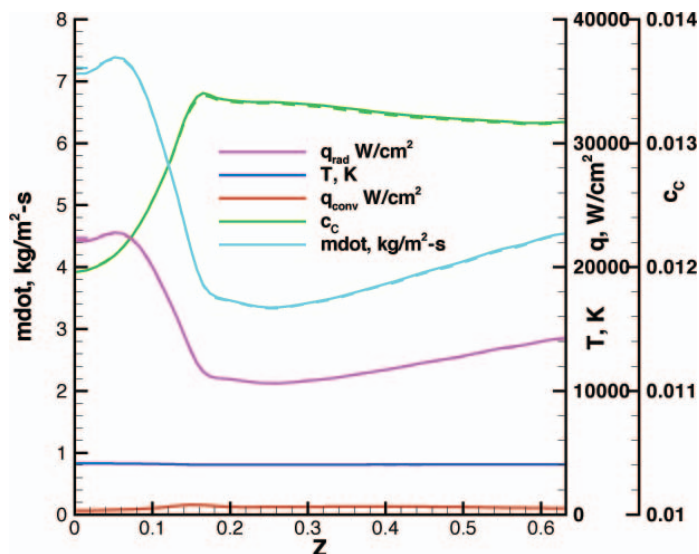

Figure 8. Mass loss rate $\dot{m}$ (cyan), atomic Carbon mass fraction c_C (green), surface temperature (blue), convective heating (red), and radiative heating (purple) at 51.16 s (peak heating) for the Galileo probe simulation. The use of film coefficient approximation (solid line) is in excellent agreement with the new boundary condition implementation (dashed line).

C. 10 km/s at Ground Level

Conceptual ideas for launching small satellites from the ground using electromagnetic ring accelerators require a thermal protection system for the carrier vehicle projectile (CVP) capable of withstanding the aerothermal environment associated with a velocity of approximately 10 km/s at ground level densities.[22, 23] Exploratory simulations are executed here to shake out any numerical issues associated with the large ablation rates computed for these environments. Similar studies have been engaged for related concepts.[24] The main result of this section is that the boundary relaxation algorithm worked without problem in this challenging simulation.

The vehicle proposed here, derived from earlier concepts,[25, 26] is a 7 deg. spherically capped cone with

American Institute of Aeronautics and Astronautics
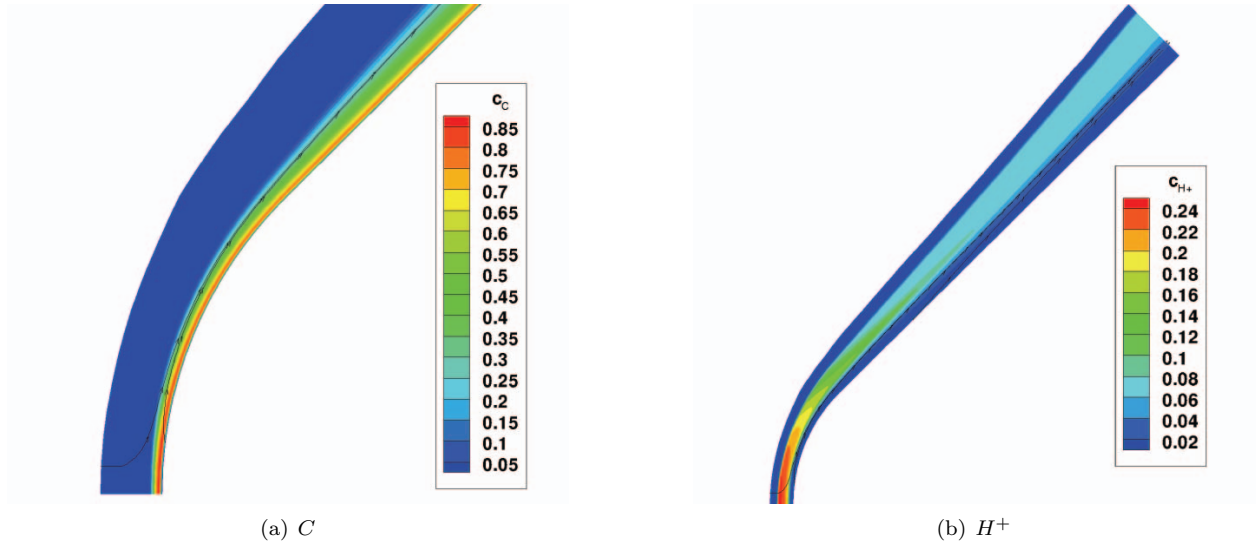
(a) C

(b) H^+

Figure 9. Contours of atomic Carbon and ionized atomic Hydrogen indicating extent of the blown gas layer and inviscid layer including streamlines from the free stream and from the body for Galileo.

5 cm nose radius and 3 meter length. Free stream conditions at ground level are: $V_\infty = 10000$ m/s, $\rho_\infty = 1.225$ kg/m^3, and $T_\infty = 288.1$ K. The flow field is resolved with 60 cells around the body and 64 cells across the shock layer. Twenty-six species for products of high temperature air and products from an Avcoat ablator include: N, O, N_2, O_2, NO, N^+, O^+, N_2^+, O_2^+, NO^+, e^-, C, C^+, CO, CO_2, C_2, C_3, C_2H, CN, H, H^+, H_2, C_2H_2, C_5, HCN, CH. The elemental mass fractions of pyrolysis gases are specified: $\tilde{c}_C = 0.547$, $\tilde{c}_H = 0.093$, $\tilde{c}_O = 0.341$, and $\tilde{c}_N = 0.019$. The elemental mass fraction of the char is $\tilde{c}_C = 1.0$. The char density is 256.3 kg/m^3. The virgin ablator density is 544.6 kg/m^3. (We make no assertion that this is the right ablator for this task or that steady-state ablation is an appropriate approximation - these are simply starting points for this study.) Both thermochemical equilibrium and non-equilibrium models have been tested. Only the equilibrium results are presented with coupled radiation and turbulent boundary layer.

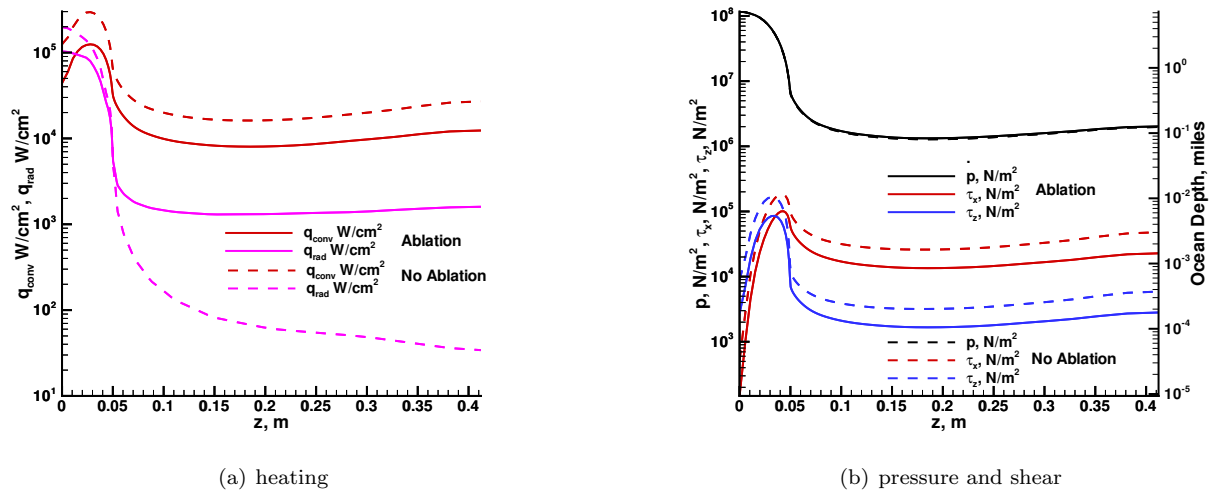(a) heating

(b) pressure and shear

Figure 10. Comparison of aerothermal loads with and without ablation for the carrier vehicle projectile (CVP).

The severity of 10 km/s at ground level should not be understated. Consider the environments described
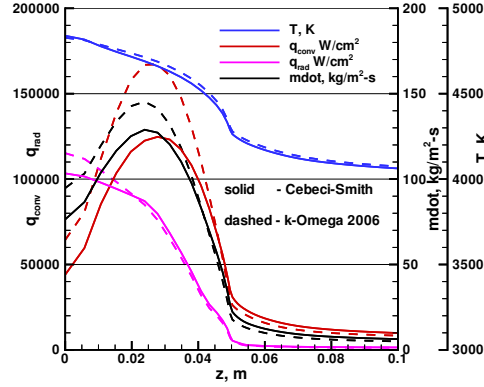
Figure 11. Mass loss rate $\dot{m}$ (black), surface temperature (blue), convective heating (red), and radiative heating (violet) for the carrier vehicle projectile (CVP) using two different turbulence models.

in Fig. 10 which highlights the changes to heating and shear associated with ablation. First note that pressure distributions are insensitive to ablation. The stagnation pressure in Fig. 10(b) at 116 million N/m^2 (116 MPa, 16824 lbf/in^2) is equivalent to the pressure at a depth of over 7 miles below sea level in the ocean. The pressure on the seven degree conical section rapidly drops to approximately 2 million N/m^2 (2 MPa, 290 lbf/in^2) which is equivalent to the pressure at a depth of 0.1 miles below sea level in the ocean. Shear stresses drop by approximately a factor of two due to the presence of ablation. The peak shear occurs near the sphere cone junction. Peak radiative heating levels occur at the stagnation point (Fig. 10(a)). The Cebeci-Smith algebraic turbulence model is applied everywhere (transition begins at the stagnation point) and so the peak convective heating levels occur just ahead of the sphere cone junction. The peak heating levels are more than a factor of 10 higher than the peak radiative heating encountered in the previous Galileo simulation (Fig. 8). Note that convective heating drops by an approximate factor of two due to ablation. The radiative heating with ablation is less than the non-ablating case in the stagnation region but is larger than the non-ablating case over the cone flank. This increase is associated with the presence of high temperature ablation products in the shock layer. These higher radiative heating levels are still almost a factor 10 less than the corresponding convective heating levels on the flank. The flank total heating levels are slightly less than the peak Galileo levels in Fig. 8. However, the Galileo pressure level at the peak heating location (not shown) is approximately a factor of 4 lower than the CVP pressure level on the flank.

Fig. 11 shows mass loss rate $\dot{m}$ in black, the surface temperature in blue, convective heating in red and radiative heating in violet for two turbulence models. There is no basis to assign uncertainty to any of these results; the two turbulence models are tested to provide an initial assessment of sensitivity. The baseline algebraic Cebeci-Smith model is shown with solid lines and Wilcox's k-omega model (2006) with compressibility correction is shown with dashed lines.The stagnation point heating is 45000 to 65000 W/cm^2 and the associated blowing rate is 75 to 95 kg/m^2-s, depending on the turbulence model. The largest difference between the models is just ahead of the sphere-cone junction where the Cebeci-Smith model is at 125000 W/cm^2 and the k-omega model is at 170000 W/cm^2. The associated peak blowing rate varies from approximately 125 to 145 kg/m^2-s. A shape change computation has not been attempted for this case but it is interesting to note that an 1800 kg/m^3 carbon-carbon ablator would experience an 8 cm/s recession rate - not counting any mechanical erosion. The k-omega results are thought to be too high because the model admits some production of turbulent kinetic energy behind the normal shock in this case. The stagnation point radiative heating levels are 103000 to 115000 W/cm^2. The surface temperature is relatively insensitive to the turbulence model and varies from approximately 4800 K at the stagnation point to 4100 K on the flank.

While the magnitude of the blowing rate is very large in this example the peak dimensionless value of $\dot{m}/(\rho_\infty V_\infty)$ is only 0.0118 which is approximately the stagnation point value of the IRV2 at trajectory point 8. Consequently, the blown gas layer sits very close to the body. The blowing rate is high but the pressure is also high which limits the extent of the ablated gases. For example, the shock standoff distance over the

American Institute of Aeronautics and Astronautics

50 mm radius body is 15.12 mm at the sphere-cone junction. (Cebeci-Smith turbulence model) The dividing streamline separating free-stream gases from ablated gases is 0.42 mm above the surface. There are 34 cells stretched across this inner portion of the boundary layer. The mesh size at the wall is 1.16 10^{-4} mm.

The design of a CVP will require a more comprehensive coupled material response - one that includes effects of temperature on compressive strength. Like the earlier IRV2 simulations, the vehicle is not "born" with a steady state ablation condition. The initial heating and shear loads will not be moderated by an ablating boundary condition. As altitude increases, free-stream density and velocity decrease and so the most severe conditions persist only on the order of seconds. A nose tip must be formulated that will be consumed by the flight environment in a predictable manner, lasting just long enough to protect the CVP flank and payload until it exits the sensible atmosphere. The flank of the CVP also sees severe aerothermal loads but these loads are not too dissimilar from those encountered in the Galileo probe. These engineering tasks are challenging but no show-stoppers are evident at this early stage.

VI.   Concluding Remarks

A relaxation algorithm to implement equilibrium, steady-state ablation boundary conditions is defined and tested for the purpose of providing strong coupling with a hypersonic flow solver. The objective is to remove correction factors or film cooling approximations that are usually applied in uncoupled or loosely coupled implementations of the flow solver and the ablation response. Three test cases are considered - the IRV-2, the Galileo probe, and a notional slender, blunted cone (carrier vehicle projectile, CVP) launched at 10 km/s from the Earth's surface. The algorithm recognizes that critical elements of the computed boundary condition, the vapor pressure of carbon at the surface and the magnitude of the blowing rate, can vary by orders of magnitude as a function of surface temperature. Robust convergence of the linearized set of boundary conditions in this circumstance may be compromised. Consequently, a successive substitution is employed and the order of succession is varied as a function of surface temperature to obtain converged solutions. The algorithm is tested under the assumption of equilibrium, steady-state ablation. This approximation introduces some simplifications into the surface energy balance that obviates a need to engage a material response code. In future work, coupling with material response code requires minor changes to the surface energy balance equation and no significant change to the present boundary condition relaxation is anticipated. In like manner for future work, non-equilibrium ablation conditions will require replacement of partial equilibrium relations with species continuity in the boundary condition equation set.

The implementation is tested on a specified trajectory for the IRV-2 to compute shape change under the approximation of steady-state ablation and one-dimensional material response with a shock layer in thermochemical non-equilibrium. This trajectory involved surface temperature variations that tested all options in the temperature dependent relaxation algorithm. A convergence history for each point of the trajectory is presented. Convergence for each point was achieved in 15000 to 30000 relaxation steps, including 10 grid adaptations during the first 5000 steps using a boundary condition relaxation factor $\epsilon = 0.001$. Two TPS densities were tested to investigate issues associated with instabilities arising from shape change. An approximate stability analysis indicates that instabilities arise from the dependence of the recession rate on local perturbations to the body surface contour as opposed to absolute levels of recession rate. A four-cell stencil is defined to enhance stability of the explicit shape change algorithm. Comparisons are made to a previous study which shows, not surprisingly, that a steady-state ablation approximation over-predicts the recession rate with largest differences encountered early in the trajectory.

A simulation on the Galileo probe, in which the heating rate is almost entirely due to radiation with the boundary layer completely blown off the body, was implemented with 16 species in thermochemical equilibrium. Fully coupled radiation and an algebraic Cebeci-Smith turbulence model were engaged for this case. Comparisons to an earlier result using film coefficient B-prime approximation showed excellent agreement with the new relaxation algorithm.

The last simulation addressed a most extreme case, 10 km/s at sea level, to test the boundary relaxation algorithm at very high blowing rates. The case describes a notional concept for a carrier vehicle projectile (CVP) flung into orbit from an electromagnetic ring launcher. Here again, the solution exhibits good convergence with specifications of an Avcoat ablator including 26 species in thermochemical equilibrium, radiation, and a coupled algebraic or two-equation turbulence model. Stagnation pressures on the order of 116 MPa and peak heating rates in excess of 125000 W/cm^2 are computed for this case.

Appendix - Shape Change Stability Analysis

Inspection of Fig. 3 suggests a correlation between the appearance of compression surfaces and localized hot spots. If one passes a reference plane through any subsection of the ablating nose using least squares fitting with perpendicular offsets[27] one notes that, relative to this reference plane, valleys and falling surfaces (expansions) tend to exhibit lower heating while peaks and rising surfaces (compressions) tend to exhibit higher heating. The correlation is imperfect and degrades as features grow and become more jagged - engaging non-linear interactions more strongly or feeling effects of upstream shock curvature. Still, the initial behavior suggests a simple analytic model for evaluating the stability of shape change.

Consider two-dimensional flow over an ablating surface. A plane is fit through a segment of the surface and surface deformations are defined locally by $y(x)$ where y is measured relative to the plane and x varies between 0 and 2π as shown in Fig. 12. Assume that the recession rate $\dot{y}$ can be expressed as a function of an average recession rate over the segment, $\dot{y}_0$, with perturbations to this average average recession rate defined as a function of local slope and curvature. Thus,

$$\dot{y} = a\frac{d^2y}{dx^2} + b\frac{dy}{dx} + \dot{y}_0 \tag{30}$$
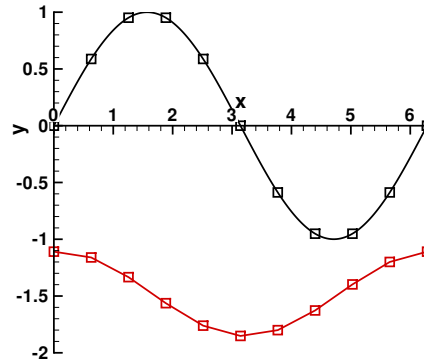
Figure 12. Response of notional, sinusoidal surface perturbation to ablation. Black lines and symbols refer to original surface and surface nodes at $t = 0$. Red lines and symbols refer to receded surface and nodes at $t = 0.4935$.

The analytic solution to Eq.30 is given by

$$y(x,t) = \dot{y}_0 t + \sum_{n=0}^{N} e^{-an^2 t}\left(\tilde{A}_n \cos(n(x+bt)) + \tilde{B}_n \sin(n(x+bt))\right) \tag{31}$$

and the initial shape $y(x,0)$ may be defined with a Fourier series. The requisite assumption of periodic continuation of surface deformations to adjacent segments with trigonometric basis functions is unrealistic but the simplification enables some insights into stability of the explicit shape change algorithm. As an example, consider the solution to Eq. 30 with $a = 2$, $b = 3$, $\dot{y}_0 = -3$ with $y(x,0) = \sin(x)$, the black line in Fig. 12. The red line indicates the solution at $t = 0.4935$. In this example, the features of the black curve have moved to the left a distance bt, the wave amplitude has decreased by a factor e^{-at}, and average level of the curve has receded to $y = \dot{y}_0 t$. If $a < 0$ on a segment then the the recession rate in valleys is larger than the recession rate on peaks; consequently, peaks are not ablated as quickly as valleys and the amplitude of perturbations grow. If $a > 0$ then the amplitude of surface perturbations goes to zero and the recession proceeds at a constant rate $\dot{y}_0$. A numerical solution of Eq.30 using backward-time, centered-space discretization is subject to the same stability limits on time step as the wave equation and heat conduction equation - $\Delta t < \min(\frac{\Delta x}{b}, \frac{\Delta x^2}{2a})$. In this idealized problem the stability of an explicit shape change algorithm is therefore not a function of the average recession rate $\dot{y}_0$ but instead is a function of the magnitude of perturbations of the recession rate relative to perturbations in the body shape.

American Institute of Aeronautics and Astronautics

A semi-analytic solution to Eq.30 can be generated using Eq. 31 that has no time step constraints. It exploits the fact that the parameters a, b, and $\dot{y}_0$ are constant in time and it generates a Fourier series to recompute constants $\tilde{A}_n$ and $\tilde{B}_n$ for the perturbed shape after each time step. Preliminary attempts to extend this idea to evaluate shape change in LAURA have failed to produce a robust algorithm. The failures stem from the underlying assumption that the variation of localized heating rates can be described strictly as a function of local surface perturbations. One finds that least squares fits to recession rates on a segment can yield negative values for a and that the constants a, b, and $\dot{y}_0$ change rapidly and erratically from one segment to the next. While there may yet be a filtering algorithm to overcome these challenges some simple updates based on these ideas have served to enhance stability of the explicit shape change algorithm.

The axisymmetric version of the shape change algorithm is defined here. Multi-dimensional extensions are theoretically obvious but have not yet been programmed or tested. Every node on the surface is updated as a function of two neighboring nodes to the right and left (five nodes along the surface defining four cell walls along the surface). Determine the equation of a reference line passing through these five nodes according to the least squares - perpendicular offsets algorithm.[27] Compute the area average blowing rate over the four cell faces.

$$\bar{\dot{m}}_{i+1/2} = \left(\sum_{j=i-1}^{j=i+2} \dot{m}_j A_j \right) / \left(\sum_{j=i-1}^{j=i+2} A_j \right) \tag{32}$$

The recession at node $i + 1/2$ is now given by

$$\Delta n_{i+1/2} = \Delta t \bar{\dot{m}}_{i+1/2}/\rho_v \tag{33}$$

The recession $\Delta n_{i+1/2}$ is made in a direction normal to the reference line described above. Evaluating displacements relative to these reference lines inhibits the formation of kinks in the surface and is consistent with the quasi-one-dimensional, steady-state ablation models used here.

References

[1]Chen, Y.-K. and Milos, F. S., "Two-Dimensional Implicit Thermal Response and Ablation Program for Charring Materials on Hypersonic Space Vehicles," AIAA Paper 2000–0206, January 2000.

[2]Kuntz, D. W., Hassan, B., and Potter, D. L., "Predictions of Ablating Hypersonic Vehicles Using and Iterative Coupled Fluid/Thermal Approach," *J. Therm. and Heat Trans.*, Vol. 15, No. 2, April 2001, pp. 129–139.

[3]Moyer, C. B. and Rindal, R. A., "Finite Difference Solution for the In-Depth Response of Charring Materials Considering Surface Chemical and Energy Balances," Aerotherm Corporation, Mountain View, CA Final Report 66-7, Part II, March 1967.

[4]Chen, Y.-K. and Milos, F. S., "Ablation and Thermal Response Program for Spacecraft Heatshield Analysis," *J. Spacecraft and Rockets*, Vol. 36, No. 3, May-June 1999, pp. 475–483.

[5]Amar, A. J., Blackwell, B. F., and Edwards, J. R., "Development and Verification of a One-Dimensional Ablation Code Including Pyrolysis Gas Flow," *J. Therm. and Heat Trans.*, Vol. 23, No. 1, 2009, pp. 59–71.

[6]Gartling, D. K. and Hogan, R. E., "COYOTE II A Finite Element Computer Program for Nonlinear Heat Conduction Problems, Part I Theoretical Background," Sandia national labs.

[7]Gartling, D. K. and Hogan, R. E., "COYOTE II A Finite Element Computer Program for Nonlinear Heat Conduction Problems, Part II Users Manual," Sandia national labs.

[8]Hogan, R. E., Blackwell, B. F., and Cochran, R. J., "Application of Moving Grid Control Volume Finite Element Method to Ablation Problems," *J. Therm. and Heat Trans.*, Vol. 10, No. 2, 1996, pp. 312–319.

[9]Conti, R. J., MacCormack, R. W., Groener, L. S., and Fryer, J. M., "Practical Navier-Stokes Computation of Axisymmetric Reentry Flowfields with Coupled Ablation and Shape Change," AIAA Paper 92–0752, Jan. 1992.

[10]Gosse, R. and Candler, G., "Evaluation of Carbon-Carbon Ablation Models Using a Fully Coupled CFD Solver," AIAA Paper 2008–3908, June 2008.

[11]Johnston, C. O., Gnoffo, P. A., and Mazaheri, A., "A Study of Ablation – Flowfield Coupling Relevant to the Orion Heatshield," AIAA Paper 2009–4318, June 2009.

[12]Gnoffo, P. A., Berry, S. A., and Norman, J. W., "Uncertainty Assessments in Simulations of 2D and Axisymmetric Hypersonic Shock Wave - Turbulent Boundary Layer Interactions at Compression Corners," Tech. rep.

[13]Gnoffo, P., Johnston, C., and Thompson, R., "Implementation of Radiation, Ablation, and Free Energy Minimization Modules for Coupled Simulations of Hypersonic Flow," AIAA Paper 2009–1399, Jan. 2009.

[14]Sutton, K. and Gnoffo, P. A., "Multi-component Diffusion with Application to Computational Aerothermodynamics," AIAA Paper 98–2575, jun 1998.

[15]Milos, F. S. and Chen, Y.-K., "Comprehensive model for multicomponent ablation thermochemistry," AIAA Paper 97–0141, January 1997.

[16]Mazaheri, A., Gnoffo, P. A., Johnston, C. O., and Kleb, B., "LAURA Users Manual: 5.3-48528," NASA TM 216836, August 2010.

[17]Johnston, C. O., Hollis, B. R., and Sutton, K., "Spectrum Modeling for Air Shock-Layer Radiation at Lunar-Return Conditions," *J. Spacecraft and Rockets*, Vol. 45, No. 5, Sep.-Oct. 2008, pp. 865–878.

[18]Bartlett, E. P., "Nonsimilar Behavior of Ablating Graphite Sphere Cones," *AIAA J.*, Vol. 8, No. 5, May 1970, pp. 948–950.

[19]Lee, E. M. and et. al., "ARBES Shape Change Code (ASCC 85Q*): Technical Report and User's Manual," Acurex report.

[20]Thompson, R. A. and Gnoffo, P. A., "Implementation of a Blowing Boundary Condition in the LAURA Code," AIAA Paper 2008–1243, Jan. 2008.

[21]Milos, F. S., Chen, Y.-K., Squire, T. H., and Brewer, R. A., "Analysis of Galileo Probe Heat Shield Ablation and Temperature Data," *J. Spacecraft and Rockets*, Vol. 36, No. 3, 1999, pp. 298–306.

[22]Fiske, O. J., Ricci, M. R., Ricci, K., and Hull, J. R., "The Launch Ring - Circular EM Accelerators for Low Cost Orbital Launch," AIAA Paper 2006–7279, Sept. 2006.

[23]Hull, J. R., Fiske, J., Ricci, K., and Ricci, M., "Analysis of Levitational Systems for a Superconducting Launch Ring," 2006 applied superconductivity conference, Aug-Sept. 2006.

[24]Gosse, R. and Candler, G., "Ablation Modeling of Electro-Magnetic Launched Projectile for Access to Space," AIAA Paper 2007–1210, Jan. 2007.

[25]Fair, H. D., Coose, P., Meinel, C. P., and Tidman, D. A., "Electromagnetic Earth-to-Space Launch," *IEEE Transactions on Magnetics*, Vol. 25, No. 1, Jan. 1989, pp. 9–16.

[26]Palmer, M. R. and Dabiri, A. E., "Electromagnetic Space Launch: A Re-evaluation in Light of Current Technology and Launch Needs and Feasibility of a Near Term Demonstration," *IEEE Transactions on Magnetics*, Vol. 25, No. 1, Jan. 1989, pp. 393–399.

[27]Weisstein, E. W., "Least Squares Fitting - Perpendicular Offsets," From mathworld - a wolfram web resource. http://mathworld.wolfram.com/leastsquaresfittingperpendicularoffsets.html.